

Search for solar axions with mass around 1 eV using coherent conversion of axions into photons

Y. Inoue^{b,d}, Y. Akimoto^a, R. Ohta^a, T. Mizumoto^a,
A. Yamamoto^{c,d}, M. Minowa^{a,d,*}

^a*Department of Physics, School of Science, University of Tokyo, 7-3-1 Hongo,
Bunkyo-ku, Tokyo 113-0033, Japan*

^b*International Center for Elementary Particle Physics, University of Tokyo,
7-3-1 Hongo, Bunkyo-ku, Tokyo 113-0033, Japan*

^c*High Energy Accelerator Research Organization (KEK), 1-1 Oho, Tsukuba,
Ibaraki 305-0801, Japan*

^d*Research Center for the Early Universe (RESCEU), School of Science,
University of Tokyo, 7-3-1 Hongo, Bunkyo-ku, Tokyo 113-0033, Japan*

Abstract

A search for solar axions has been performed using an axion helioscope which is equipped with a 2.3 m-long 4 T superconducting magnet, a gas container to hold dispersion-matching gas, PIN-photodiode X-ray detectors, and a telescope mount mechanism to track the sun. A mass region around $m_a = 1$ eV was newly explored. From the absence of any evidence, analysis sets a limit on axion-photon coupling constant to be $g_{a\gamma\gamma} < 5.6\text{--}13.4 \times 10^{-10} \text{GeV}^{-1}$ for the axion mass of $0.84 < m_a < 1.00$ eV at 95% confidence level. It is the first result to search for the axion in the $g_{a\gamma\gamma}$ - m_a parameter region of the preferred axion models with a magnetic helioscope.

Key words: solar axion, helioscope, PIN photodiode, superconducting magnet
PACS: 14.80.Mz, 07.85.Fv, 96.60.Jw

* Corresponding author

Email address: minowa@phys.s.u-tokyo.ac.jp (M. Minowa).

1 Introduction

Quantum chromodynamics (QCD) is the theory of the strong interactions. Although QCD has proven remarkably successful, there is a blemish called the strong CP problem. The strong CP problem is that the effective Lagrangian of QCD has CP violating term but it is not observed, i.e., the experimental value of neutron electric dipole moment is smaller than expected by many orders of magnitude. Peccei and Quinn proposed an attractive solution to solve this problem [1–5]. They introduced a new global $U(1)$ symmetry, Peccei–Quinn (PQ) symmetry. When PQ symmetry is spontaneously broken, a new effective term arises in QCD Lagrangian which cancels the CP violation term. The solution also predicts a new pseudo Nambu–Goldstone boson, axion. The expected behavior of an axion is characterized mostly by the scaling factor of the PQ symmetry breaking, f_a , and so its mass, m_a , which is directly related to f_a by $m_a = 6 \times 10^{15} [\text{eV}^2]/f_a$.

Axions are expected to be produced in stellar core through their coupling to photons with energies of order keV. Especially, the sun can be a powerful source of axions and the so-called ‘axion helioscope’ technique may enable us to detect such axions directly [6,7].

The principle of the axion helioscope is illustrated in Fig. 1. Axions would be produced through the Primakoff process in the solar core. The differential flux of solar axions at the Earth is approximated by [8,9]

$$\begin{aligned} d\Phi_a/dE = & 6.020 \times 10^{10} [\text{cm}^{-2}\text{s}^{-1}\text{keV}^{-1}] \\ & \times \left(\frac{g_{a\gamma\gamma}}{10^{-10}\text{GeV}^{-1}} \right)^2 \left(\frac{E}{1\text{keV}} \right)^{2.481} \exp \left(-\frac{E}{1.205\text{keV}} \right), \end{aligned} \quad (1)$$

where $g_{a\gamma\gamma}$ is the axion-photon coupling constant¹. Their average energy is 4.2 keV reflecting the core temperature of the sun. Then, they would be coherently converted into X-rays through the inverse process in a strong magnetic field at a laboratory. The conversion rate is given by

$$P_{a \rightarrow \gamma} = \left| \frac{g_{a\gamma\gamma}}{2} \exp \left[-\int_0^L dz \Gamma/2 \right] \times \int_0^L dz B_\perp \exp \left[i \int_0^z dz' \left(q - \frac{i\Gamma}{2} \right) \right] \right|^2, \quad (2)$$

where z and z' are the coordinate along the incident solar axion, B_\perp is the strength of the transverse magnetic field, L is the length of the field along z -axis, Γ is the X-ray absorption coefficient of helium, $q = (m_\gamma^2 - m_a^2)/2E$ is

¹ The formula is different from the one in our previous paper [10,11], but both coincide numerically with good approximation.

the momentum transfer by the virtual photon, and m_γ is the effective mass of the photon which equals zero in vacuum. Eq. (2) is reduced to

$$P_{a \rightarrow \gamma} = \left(\frac{g_{a\gamma\gamma} B_\perp L}{2} \right)^2 \left[\frac{\sin(qL/2)}{qL/2} \right]^2, \quad (3)$$

in case q and B_\perp is constant along z -axis and $\Gamma = 0$.

In 1997, the first phase measurement [10] was performed using an axion helioscope with a dedicated superconducting magnet which is identical to the one used in the present experiment, except that the gas container was absent and the conversion region was vacuum. Its sensitivity was limited to the axion mass region of $m_a < 0.03 \text{ eV}$ due to a loss of coherence by non-zero q in Eq. (3).

If one can adjust m_γ to m_a , coherence will be restored for non-zero mass axions. This is achieved by filling the conversion region with gas. A photon in the X-ray region acquires a positive effective mass in a medium. In light gas, such as hydrogen or helium, it is well approximated by

$$m_\gamma = \sqrt{\frac{4\pi\alpha N_e}{m_e}}, \quad (4)$$

where α is the fine structure constant, m_e is the electron mass, and N_e is the number density of electrons. We adopted cold helium gas as a dispersion-matching medium. Here, light gas was preferred since it minimizes self absorption by gas. It is worth noting that helium remains at gas state even at 5–6 K, the operating temperature of our magnet. Since the bore of the magnet is limited in space, the easiest way is to keep the gas at the same temperature as the magnet. Moreover, axions as heavy as a few electronvolts can be reached with helium gas of only about one atmosphere at this temperature.

In this way, in 2000, the second phase measurement [11] was performed to search for sub-electronvolt axions. This experiment, together with the first phase measurement of 1997 [10] with vacuum conversion region, yielded an upper limit of $g_{a\gamma\gamma} < 6.0\text{--}10.5 \times 10^{-10} \text{ GeV}^{-1}$ (95% CL) for $m_a < 0.27 \text{ eV}$.

In this paper, we will present the result of the third phase measurement in which we scanned the mass region between $0.84 < m_a < 1.00 \text{ eV}$ using the upgraded apparatus to withstand higher pressure gas.

2 Experimental apparatus

The schematic figure of the axion helioscope is shown in Fig. 2. It is designed to track the sun in order to achieve long exposure time. It consists of a superconducting magnet, X-ray detectors, a gas container, and an altazimuth mounting. In the following paragraphs, we will describe each part in due order.

The superconducting magnet [12] consists of two 2.3-m long race-track shaped coils running parallel with a 20-mm wide gap between them. The magnetic field in the gap is 4 T perpendicular to the helioscope axis. The coils are kept at 5–6 K during operation. In order to make it easy to swing this large cryogenic apparatus, two devices are engaged. First, the magnet was made cryogen-free by making two Gifford-McMahon refrigerators to cool it directly by conduction. Second, a persistent current switch was equipped. Thanks to this, the magnet can be freed from thick current leads after excitation, and the magnetic field is very stable for a long period of time without supplying current.

The container to hold dispersion-matching gas is inserted in the $20 \times 92 \text{ mm}^2$ aperture of the magnet. Its body is made of four 2.3-m long 0.8-mm thick stainless-steel square pipes welded side by side to each other. The entire body is wrapped with 5N high purity aluminium sheet to achieve high uniformity of temperature. The measured thermal conductance between the both ends was $1 \times 10^{-2} \text{ W/K}$ at 6 K. One end at the forward side of the container is sealed with welded plugs and is suspended firmly by three Kevlar cords, so that thermal flow through this end is highly suppressed. The opposite side nearer to the X-ray detectors is flanged and fixed to the magnet. At this end of the container, gas is separated from vacuum with an X-ray window manufactured by METOREX which is transparent to X-ray above 2 keV and can hold gas up to 0.3 MPa at liquid helium temperature.

To have automatic sequential pressure settings of the dispersion-matching gas for the scan of the axion mass region around 1 eV, a gas handling system is built with 3 Piezo valves (two HORIBASTECH PV1101 and a PV1302) and a precision pressure gauge (YOKOGAWA MU101-AH1N). The temperature of the gas container was measured by a Lakeshore CGR thermistor.

Required pressure for a given mass was determined by the corresponding gas density and the temperature based on interpolation of the tables from NIST [13]. The error of the target mass is estimated to be less than 5 meV by the errors of the pressure and the temperature. Since we are scanning a range of the axion mass, the error is only crucial to the lower and upper edges of the mass range.

Helium gas is fed to the container through the Piezo valve to have a specified

pressure setting. If a lower pressure setting is required, then another Piezo valve is opened to suck the gas by a vacuum pump connected to the valve. Once a proper pressure setting is settled, all the valves are closed and the helium gas is kept confined to have a constant electron number density in the container until the measurement for the setting is completed. The uniformity of the temperature guarantees the homogeneous density along the length of the container. The whole process is done step by step automatically to scan the axion mass.

Absorption of X-ray in the helium gas is not negligible and the effect is properly calculated in Eq. (2). The electron number density might vary slightly along the container from the one end to the other because of the gravity when the inclination is high, and the coherence could be partly lost accordingly. The effect is also taken into account in Eq. (2). The decreases of the conversion probability $P_{a \rightarrow \gamma}$ due to the absorption and the gravity are less than 23% and 1% , respectively when m_γ is tuned to 1.0 eV at the center of the gas container.

For emergency exhaust of the gas in case of rapid temperature increase due to a magnet quenching, a rapture disk, which is designed to break at 0.248 MPa, is introduced into the gas handling system to avoid destruction of the X-ray window by the over pressure.

Sixteen PIN photodiodes, Hamamatsu Photonics S3590-06-SPL, are used as the X-ray detectors, whose chip sizes are $11 \times 11 \times 0.5 \text{ mm}^3$ each. In the present measurement, however, twelve of them are used for the analysis because four went defective through thermal stresses since the measurement of the previous phase. The effective area of a photodiode was measured formerly using a pencil-beam X-ray source, and found to be larger than $9 \times 9 \text{ mm}^2$. It has an inactive surface layer of $0.35 \mu\text{m}$ [15]. Each chip is mounted on a Kapton film bonded to an Invar plate with cryogenic compatible adhesive. The X-ray detectors are mounted in a 10-mm thick radiation shielding box made of oxygen-free high conductivity copper (OFHC Cu), which is then surrounded by a lead shield of about 150 mm thick. The copper shield is operated at about 60 K, so that it also functions as a cold finger for the X-ray detectors. Details on the X-ray detector are given in Ref. [14,15].

The output from each photodiode is fed to a charge sensitive preamplifier whose first-stage FET is at the cryogenic stage near the photodiode chip and the preamplifier outputs are digitized using CAMAC flash analog-to-digital convertors (FADC's), REPIC RPC-081's, at a sampling rate of 10 MHz. The preamplifier outputs are also fed to shaping amplifiers, Clear Pulse CP4026, whose outputs are then discriminated to generate triggers. Thus, waveforms of the sixteen preamplifier outputs are recorded simultaneously over $50 \mu\text{s}$ before and after each trigger to be committed to later off-line analysis. Each detector was calibrated by 5.9-keV Mn X-rays from a ^{55}Fe source installed in front of

them. The source is manipulated from the outside and is completely retracted behind the shield during the axion observations.

The entire axion detector is constructed in a vacuum vessel and the vessel is mounted on an altazimuth mount. Its trackable altitude ranges from -28° to $+28^\circ$ and its azimuthal direction is designed to be limited only by a limiter which prevents the helioscope from endless rotation. However, in the present measurement, the azimuthal range is restricted to about 60° because a cable handling system for its unmanned operation is not completed yet. The range corresponds to an exposure time of about a quarter of a day in observing the sun. This is enough for the time being, since background is measured during the other three quarters of a day. When the entire cable handling system is complete, running time per pressure setting can be shortened by a factor of more than two.

This helioscope mount is driven by two AC servo motors controlled by a computer (PC). The PC also monitors the azimuthal and altitudinal directions of the helioscope regularly by two precision rotary encoders and forms a feedback controlling loop as a whole. The U.S. Naval Observatory Vector Astronomy Subroutines (NOVAS) [16] were used to calculate the solar position. The altitudinal origin was determined from a spirit level. While the sun is not directly visible from the laboratory in the basement floor, the azimuthal origin was first determined by a gyrocompass, which detects the north direction by the rotation of the earth within an error of $\pm 8''$, and then it was introduced to the laboratory with a theodolite.

Since the effective aperture of the helioscope is narrow, it is crucial to determine its accurate geometry. The axis of the helioscope is defined by two cross hairs at the edge of the vacuum vessel. The position of each part of the helioscope was measured relative to these cross hairs from their exterior using the theodolite when they were installed. The positions of the PIN photodiodes were determined relative to the copper shielding box from a photo image taken prior to the installation. As it is hard to estimate analytically the effect of the geometrical errors as well as the effect of the size of the axion source, we performed a Monte Carlo simulation and found that the overall effective area is larger than 371 mm^2 at 99% confidence level.

3 Measurement and Analysis

From December 2007 through April 2008, a measurement employing dispersion-matching gas was performed for 34 photon mass settings with about three days of running time per setting to scan around 1 eV, which is shown in Table 1.

Before obtaining energy spectra, each event was categorized into two major groups, the solar observation and the background. Events while the measured direction agreed with the sun are counted as former. When the sun is completely out of the magnet aperture, events are counted as latter. Otherwise events are discarded.

We performed numerical pulse shaping to the raw waveforms using the Wiener filter. The energy of an X-ray is given by the peak height of a wave after the shaping. The shaped waveform is given by

$$U(\omega) = \frac{S^*(\omega)C(\omega)}{|N(\omega)|^2}, \quad (5)$$

where $U(\omega)$, $S(\omega)$, $C(\omega)$, and $N(\omega)$ are Fourier transformations of the shaped waveform, the ideal signal waveform, the measured waveform, and the noise, respectively. Noises are obtained by gathering waveforms while no trigger exists, and the ideal signal waveform is approximated by averaging signals from 5.9-keV X-rays. The response function of this waveform analysis, i.e., non-linearity, gain walk by trigger timing, etc., was investigated thoroughly using simulated pulses which were obtained by adding the template waveform to the noise waveforms. A correction was made based on this numerical simulation. Saturation arose at about 25 keV, therefore, $E > 20$ keV was not used in the later analysis.

Event reduction process is applied in the same way as the second phase measurement [11] in order to get rid of bad events like microphonics. Applying the same cuts to the ^{55}Fe source data, we found the loss of axion detection efficiency by the reduction to be less than 1.5%.

The background level was about $1.0 \times 10^{-5} \text{keV}^{-1} \text{s}^{-1} / \text{PIN}$ at $E = 5\text{--}10$ keV. By analysing the calibration data, we found the energy resolution of each photodiode to be 0.8–1.2 keV (FWHM) for 5.9-keV photons.

In Fig. 3, the energy spectrum of the solar observation with the gas density for $m_\gamma = 1.004$ eV is shown together with the background spectrum. We searched for expected axion signals which scale with $g_{a\gamma\gamma}^4$ for various m_a in these spectra. The smooth curve in the figure represents an example for the expected axion signal where $m_a = m_\gamma = 1.004$ eV and $g_{a\gamma\gamma} = 7.7 \times 10^{-10} \text{GeV}^{-1}$, which corresponds to the upper limit estimated as follows.

A series of least χ^2 fittings was performed assuming various m_a values. Data from the 34 different gas density settings were combined by using the summed χ^2 of the 34. The energy region of 4–20 keV was used for fitting where the efficiency of the trigger system is almost 100% and the FADCs do not saturate. As a result, no significant excess was seen for any m_a , and thus an

upper limit on $g_{a\gamma\gamma}$ at 95% confidence level was given following the Bayesian scheme. Fig. 4 shows the limit plotted as a function of m_a . Our previous limits from the first [10] and the second [11] phase measurements and some other bounds are also plotted in the same figure. The shown previous limits have been updated using newly measured inactive surface layer thickness of the PIN photodiode [15]; the difference is, however, marginal. The SOLAX [18], COSME [19] and DAMA [20] are solar axion experiments which exploits the coherent conversion on the crystalline planes in a germanium and a NaI detector. The experiment by Lazarus et al. [17] and CAST [22] are the same kind of experiments as ours. The latter utilizes large decommissioned magnets of the LHC at CERN. Its limit is better than our previous limits by a factor of seven in low m_a region due to its larger B and L in Eq. (3). In the region $m_a > 0.14$ eV, however, our previous and present limits surpass the limit of CAST. The limit $g_{a\gamma\gamma} < 2.3 \times 10^{-9} \text{GeV}^{-1}$ is the solar limit inferred from the solar age consideration and the limit $g_{a\gamma\gamma} < 1 \times 10^{-9} \text{GeV}^{-1}$ is a more stringent limit reported by Schlattl et al. [21] based on comparison between the helioseismological sound-speed profile and the standard solar evolution models with energy losses by solar axions. Watanabe and Shibahashi [23] have argued that the helioseismological bound can be lowered to $g_{a\gamma\gamma} < 4.0 \times 10^{-10} \text{GeV}^{-1}$ if the ‘seismic solar model’ and the observed solar neutrino flux are combined.

4 Conclusion

The axion mass around 1 eV has been scanned with an axion helioscope with cold helium gas as the dispersion-matching medium in the $4 \text{ T} \times 2.3 \text{ m}$ magnetic field, but no evidence for solar axions was seen. A new limit on $g_{a\gamma\gamma}$ shown in Fig. 4 was set for $0.84 < m_a < 1.00$ eV. It is the first result to search for the axion in the $g_{a\gamma\gamma}$ - m_a parameter region of the preferred axion models [24] with a magnetic helioscope.

When the complete unmanned operation is ready with the automatic cable handling system, the mass scan will be continued to cover still wider mass range around 1 eV.

Acknowledgements

The authors thank the former director general of KEK, Professor H. Sugawara, for his support in the beginning of the helioscope experiment. This research was partially supported by the Japanese Ministry of Education, Science, Sports and Culture, Grant-in-Aid for COE Research and Grant-in-Aid for Scientific Research (B), and also by the Matsuo Foundation.

References

- [1] R.D. Peccei, H.R. Quinn, Phys. Rev. Lett. 38 (1977) 1440.
- [2] R.D. Peccei, H.R. Quinn, Phys. Rev. D 16 (1977) 1791.
- [3] S. Weinberg, Phys. Rev. Lett. 40 (1978) 223.
- [4] F. Wilczek, Phys. Rev. Lett. 40 (1978) 279.
- [5] J.E. Kim, Phys. Rep. 150 (1987) 1.
- [6] P. Sikivie, Phys. Rev. Lett. 51 (1983) 1415; 52 (1984) 695 (erratum).
- [7] K. van Bibber et al., Phys. Rev. D 39 (1989) 2089.
- [8] J. N. Bahcall and M. H. Pinsonneault, Phys. Rev. Lett. 92 (2004) 121301.
- [9] G. G. Raffelt, Contribution to XI International Workshop on “Neutrino Telescope”, Venice, Italy, Feb. 22–25. 2005.
- [10] S. Moriyama et al., Phys. Lett. B 434 (1998) 147.
- [11] Y. Inoue et al., Phys. Lett. B 536 (2002) 18.
- [12] Y. Sato et al., Development of a Cryogen-free Superconducting Dipole Magnet, in: Proc. of the 15th International Conference on Magnet Technology (MT-15) (Beijing, October 1997), eds.: L. Liangzhen, S. Guoliao, Y. Luguang (Science Press, Beijing, 1998) pp. 262–265; KEK-Preprint-97-202 (November, 1997).
- [13] Vincent D. Arp and Robert D. McCarty, Thermophysical Properties of Helium-4 from 0.8 to 1500 K with Pressures to 2000 MPa, NIST Technical Note 1334, (U.S. Department of Commerce, National Technical Information Service, 1989).
- [14] T. Namba et al., Nucl. Instr. Meth. A 489 (2002) 224.
- [15] Y. Akimoto et al., Nucl. Instr. Meth. A 557 (2006) 684.
- [16] G. H. Kaplan et al., Astronomical Journal 97 (1989) 1197;
URL: <http://aa.usno.navy.mil/AA/software/novas/>.
- [17] D. M. Lazarus et al., Phys. Rev. Lett. 69 (1992) 2333.
- [18] A. O. Gattone et al., Nucl. Phys. B(Proc. Suppl.)70 (1999) 59.
- [19] A. Morales et al., Astropart. Phys. 16 (2002) 325.
- [20] R. Bernabei et al., Phys. Lett. B 515 (2001) 6.
- [21] H. Schlattl, A. Weiss, G. Raffelt, Astropart. Phys. 10 (1999) 353.
- [22] K. Zioutas et al., Phys. Rev. Lett. 94 (2005) 121301, C. Eleftheriadis, arXiv:0706.0637v1, and S. Andriamonje et al. (CAST Collaboration), J. Cosmol. Astropart. Phys. 04 (2007) 010.

- [23] S. Watanabe, H. Shibahashi, hep-ph/0112012.
- [24] D. B. Kaplan, Nucl. Phys. B 260 (1985) 215, M. Srednicki, Nucl. Phys. B 260 (1985) 689, and S. L. Cheng, C. Q. Geng, W. -T. Ni, Phys. Rev. D 52 (1995) 3132.

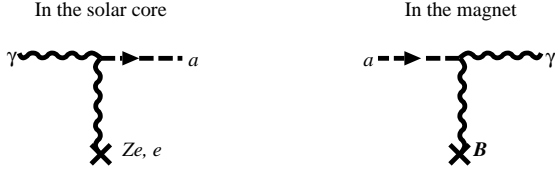


Fig. 1. The solar axions produced via the Primakoff process in the solar core are, then, converted into X-rays via the reverse process in the magnet.

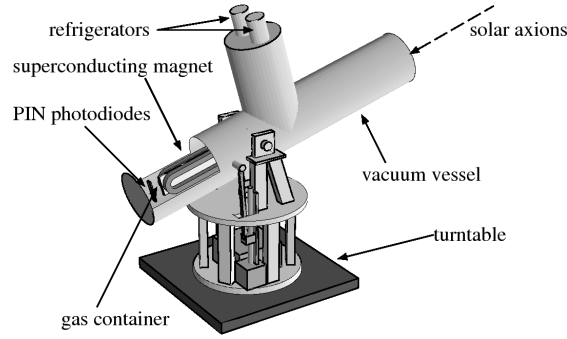


Fig. 2. The schematic view of the axion helioscope.

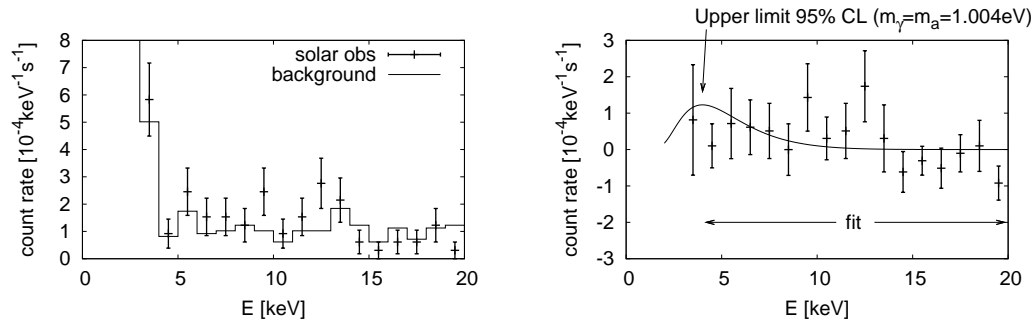


Fig. 3. The left figure shows the energy spectrum of the solar observation (error bars) and the background spectrum (solid line) when the gas density was tuned to $m_\gamma = 1.004 \text{ eV}$. The right figure shows the net energy spectrum of the left where the background is subtracted from the solar observation.

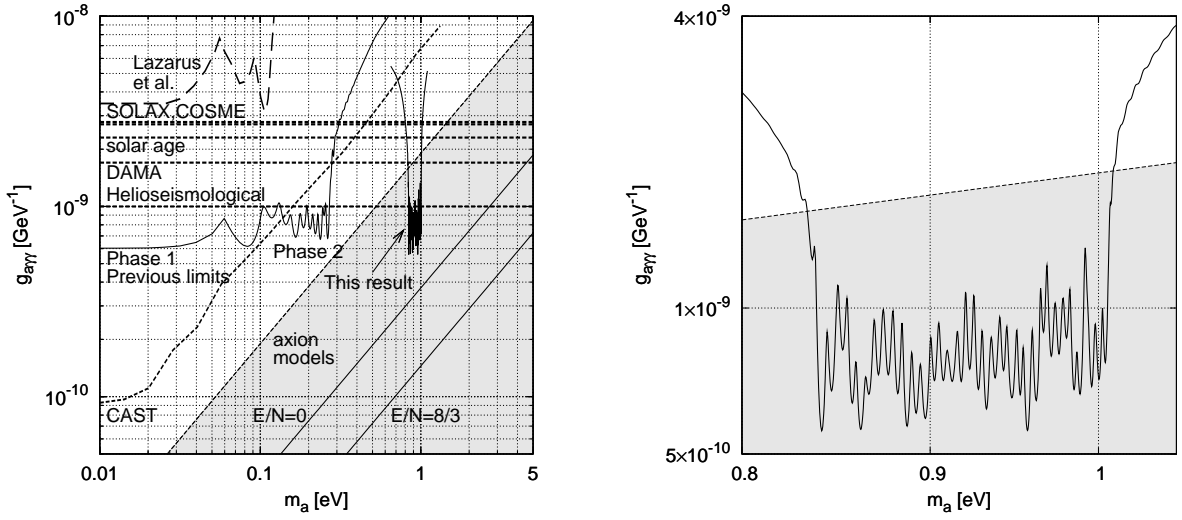


Fig. 4. The left figure is the exclusion plot on $g_{a\gamma\gamma}$ to m_a . The new limit and the previous ones[10,11] are plotted in solid lines. Dashed lines are the limit by Lazarus et al. [17], the limit by CAST experiment [22], the limit by SOLAX experiment [18], the limit by COSME experiment [19], the limit by DAMA experiment [20], the limit inferred from the solar age consideration, and the helioseismological bound. The hatched area corresponds to the preferred axion models [24]. The right figure shows the magnified view of the new limit.

molar density [mol/m ³]	m_γ [eV]	live time [s]	
		solar run	background
425.8	0.841	8726	33122
431.1	0.846	25362	97561
437.1	0.852	25916	97863
442.4	0.857	24209	91178
447.2	0.862	16724	62828
451.7	0.866	23543	92698
457.1	0.871	22070	84977
462.8	0.877	20242	78517
468.3	0.882	20508	79185
473.8	0.887	18916	73595
479.3	0.892	19569	74852
484.8	0.897	18788	72368
490.3	0.902	18801	71656
495.8	0.907	18985	71630
501.4	0.912	18343	68041
507.0	0.918	18126	67753
512.5	0.923	18022	66218
518.1	0.928	18468	68035
523.4	0.932	17805	63160
529.0	0.937	18683	66060
534.6	0.942	19309	65930
540.2	0.947	18650	63162
545.9	0.952	19801	67513
550.9	0.957	20626	68302
557.0	0.962	22478	73061
562.0	0.966	22126	66594
567.6	0.971	24790	74858
573.1	0.976	24464	69696
578.5	0.980	23120	69297
584.0	0.985	23922	73955
588.4	0.988	29533	91299
597.0	0.996	35946	110559
602.6	1.000	36503	108174
607.3	1.004	32584	97671

Table 1
Table of the gas settings and each live time.